Nanodisk-based glioma-targeted drug delivery enabled by a stable glycopeptide

Huan Wang, Xiaoyi Wang, Cao Xie, Mingfei Zhang, Huitong Ruan, Songli Wang, Kuan Jiang, Fei Wang, Changyou Zhan, Weiyue Lu, Hao Wang

PII: S0168-3659(18)30331-6
DOI: doi:10.1016/j.jconrel.2018.06.006
Reference: COREL 9330

To appear in: *Journal of Controlled Release*

Received date: 19 February 2018
Revised date: 16 May 2018
Accepted date: 4 June 2018

Please cite this article as: Huan Wang, Xiaoyi Wang, Cao Xie, Mingfei Zhang, Huitong Ruan, Songli Wang, Kuan Jiang, Fei Wang, Changyou Zhan, Weiyue Lu, Hao Wang , Nanodisk-based glioma-targeted drug delivery enabled by a stable glycopeptide. Corel (2017), doi:10.1016/j.jconrel.2018.06.006

Nanodisk-based glioma-targeted drug delivery enabled by a stable glycopeptide

Huan Wang[a,b], Xiaoyi Wang[a], Cao Xie[a], Mingfei Zhang[a], Huitong Ruan[a], Songli Wang[a], Kuan Jiang[a], Fei Wang[a], Changyou Zhan[a,c], Weiyue Lu[a,d,]**, Hao Wang[b,]*

[a]*Department of Pharmaceutics, School of Pharmacy, and Key Laboratory of Smart Drug Delivery, Fudan University, Shanghai 201203, & State Key Laboratory of Medical Neurobiology, and Collaborative Innovation Center for Brain Science, Fudan University, Shanghai 200032, China.*

[b]*National Pharmaceutical Engineering Research Center, China State Institute of Pharmaceutical Industry, Shanghai 201203, China.*

[c]*Department of Pharmacology, School of Basic Medical Sciences, Fudan University, Shanghai 200032, & State Key Laboratory of Molecular Engineering of Polymers, Fudan University, Shanghai, 200433, China.*

[d]*Department of Integrative Medicine, Huashan Hospital, Fudan University, & Institute of Integrative Medicine of Fudan University, Shanghai 200041, and Minhang Branch, Zhongshan Hospital and Institute of Fudan-Minghang Acadimic Health System, Minghang Hospital, Fudan University, Shanghai 201199, China.*

* Conrespondence to: Hao Wang. e-mail: wanghao10@sinopharm.com; tel.: +86-21-51320211; fax: +86-21-51320728;

** Conrespondence to: Weiyue Lu. e-mail: wylu@shmu.edu.cn; tel.: +86-21-51980006; fax: +86-21-51980090.

Abstract

Heptapeptide ATWLPPR (A7R) binds specifically to vascular endothelial growth factor receptor 2 (VEGFR2) and neuropilin-1 (NRP-1) overexpressed in glioma cells, exhibiting high potential to achieve glioma targeted drug delivery. However, *in vivo* application of A7R peptide remains challenging due to the poor proteolytic stability and inaccessibility of A7R to the brain. To tackle these problems, we identified a glycosylated A7R derivative to enhance *in vivo* stability and brain transport efficacy. Our results showed that glycosylation of peptide could efficiently improve stability in serum, traverse the blood-brain barrier (BBB) and be uptaken by glioma cells. Furthermore, a novel glioma-targeted drug delivery system was constructed successfully employing glycopeptide as the targeting moiety and nanodisk as the carrier of paclitaxel (PTX). Physicochemical characterization showed that the nanodisk presented suitable size of 50 nm and adequate loading capacity of PTX. Compared to non-glycosylated nanodisk, glycopeptide modification could significantly enhance the uptake of disks by brain capillary endothelial cells through glucose transporter 1 (GLUT1). *In vivo* imaging and glioma fluorescence section results also indicated that nanodisks modified with glycopeptide showed a higher accumulation in glioma. The glycopeptide-enabled PTX delivery system exhibited superior anti-glioma efficacy in intracranial glioma xenograft model. These results suggested that glycosylation of peptides provided an efficient pathway to design multifunctional and stable brain targeting ligands.

Keywords: Glycopeptide; Nanodisk; Glucose Transporter; blood-brain barrier; Glioma

1. Introduction

Glioblastoma multiforme (GBM) is the most malignant primary brain tumor with high mortality and poor prognosis. The median survival of GBM patients after surgery is 8 to 15 months and the overall 5-year survival rate is below 5%[1.2]. Given extremely infiltrative nature of glioma, chemotherapy remains an effective adjunct treatment to surgical resection in clinic[3]. In recent years, actively targeted drug delivery systems have demonstrated the potential to improve antitumor efficacy of chemotherapeutic agents by functionalizing targeting ligands on the surface of nanocarriers. Peptide ligands have been extensively exploited for actively targeting nanomedicines due to their ease of synthesis and screening[4-7].

A mutated phage library selected peptide A7R (ATWLPPR) exhibited specific binding to vascular endothelial growth factor receptor 2 (VEGFR2) and neuropilin-1 (NRP-1), which are overexpressed in glioma cells. In our previous study, A7R-functionalized drug delivery systems have been developed for targeting subcutaneous glioma xenograft in nude mice, effectively inhibiting tumor growth[8]. However, multiple obstacles restrict the precise delivery of chemotherapeutic agents to the brain as well as the brain tumors. The A7R peptide is subject to proteolysis in blood after systemic administration. The blood-brain barrier (BBB) would present additional obstacle to brain tumor targeted delivery of A7R functionalized drug delivery systems.

Membrane transporters such as glucose transporter (GLUT) have been employed to facilitate the brain transport of drug delivery systems. GLUT1, a representative member in the GLUT family, is an endogenous transporter avidly presenting in brain microvessels[9]. D-glucose moieties are the essential fuel for the large and uninterrupted energy demand of the brain[10]. Due to this high capacity of glucose utilization and transport efficiency, glucose moieties are considered good candidates to facilitate brain delivery[11-13].

Peptides have been stabilized by different methods, including the design of retro-all-D or retro-inverso peptide analogues[14], head-to-tail cyclization[8], terminal amino acid modification and introduction of non-natural amino acids[15]. Among them, glycosylation is among the simplest and the most effective methods. Conjugation of sugar moieties to opioid peptides leads to improved bioavailability in brain, as a result of prolonged metabolic and clearance half-live[16]. N-terminal glycosylation improved the resistance of glucagon-like peptide-1 to dipeptidyl-peptidase-IV (DPP-IV) and exhibited substantially improved biological activities[17.18].

Thus, we hypothesize that the introduction of glucose moieties on A7R would be multifunctional. The stable glycopeptide may have brain and glioma dual-targeted effect. Firstly, the glycosylated A7R has better biological stability and prolonged blood circulation time *in vivo*. Then the glucose moiety enables brain transport of peptide via GLUT-mediated pathway. After entry into brain, the glycosylated A7R peptide would further target the tumor region by recognizing the overexpressed VEGFR2 and NRP-1.

Recently, polyethylene glycol (PEG)-stabilized nanodisk, formed in mixtures of phospholipids, cholesterol and PEG lipids, has received increasing interest in drug delivery. The nanodisk is a nano-sized flat circular lipid bilayer surrounded by a highly curved rim with PEG-lipids readily distributing on the rim of lipid disks. A series of linear alpha-helical peptides, such as melittin, showed high affinity for the rim of PEG-stabilized lipid disks. The melittin-loaded lipid disks significantly reduced the hemolytic effect and efficiently inhibited tumor growth in a tumor bearing mice model[19]. The PEG-stabilized disks also provided a larger

hydrophobic volume for chemotherapeutics compared to micelles and that their size could be tailored for loading different drugs[20]. DOX-loaded disks showed enhanced bioavailability and improved anticancer effect in comparison to free DOX[21].

In this work we synthesized a series of glycosylated analogues of A7R and compared their serum stability, brain and glioma targeting ability. The optimal glycosylated peptide was conjugated on the surface of nanodisk for dual-targeted drug delivery as illustrated in Scheme 1. Cellular uptake efficiency, tumor spheroid penetration, cytotoxicity and biodistribution of nanodisk formulations were investigated. The anti-glioma effects of paclitaxel-loaded nanodisk formulations were evaluated in an intracranial glioma-bearing nude mice model.

Scheme 1. Schematic illustration of glycopetide-modified nanodisk as a dual-targeted drug delivery system for anti-glioma therapy.

2. Materials and Methods

2.1 Materials and reagents

Fmoc-protected α-amino acids were supplied by GL Biochem Ltd. (Shanghai, China). Fmoc-Rink Amide MBHA resin was supplied by Xi'an innovision bioscience Co. Ltd. (Xi'an, China). Pentaacetate glucose was purchased from Aladdin (Shanghai, China). O-benzotriazole-N,N,N′,N′-tetramethyl-uronium-hexafluorophosphate (HBTU) and 1-Hydroxybenzotriazole anhydrous (HOBt) were purchased from American Bioanalytical Co. Ltd. (Massachusetts, USA). Diisopropylethylamine (DIEA) was supplied by Sigma-Aldrich (St. Louis, MO, USA). Fluorescein-5-maleimide and Cyanine7-maleimide were obtained from Fanbo Biochemicals (Beijing, China). Rat serum was supplied by Invitrogen (Grand Island, NY). Matrigerl Basement Membrane Matrix was purchased from BD Biosciences (USA). POPC (1-palmitoyl-2-oleoyl-sn-glycero-3-phosphocho-line) and mPEG2000-DSPE were purchased from Lipoid GmbH (Ludwigshafen, Germany). Cholesterol was purchased from Sinopharm Chemical Reagent Co. Ltd (Shanghai, China). Mal-PEG3400-DSPE and NH2-PEG3400-DSPE were purchased from Laysan Bio (Arab, USA). FITC was purchased from Sigma-Aldrich (St. Louis, USA). Sephadex G50 was purchased from GE Healthcare (Uppsala, Sweden). DAPI (4',6-diamidino-2-phenylindole) was supplied by Roche (Basel, Switzerland). DiR (1,1'-dioctadecyl-3,3,3′,3′-tetramethyl indotricarbocyanine iodide), DiD (1,1'-dioctadecyl-3,3,3',3'-tetramethylindodicarbocyanine, 4-chlorobenzenesulfonate salt dye) , and Paclitaxel were purchased from Meilun Biology Technology Co. Ltd. (Dalian, China). Methanol and acetonitrile were purchased from Fisher Scientific (USA). N,N-dimethyformamide (DMF), dichloromethane (DCM) and other chemical reagents were purchased from Sinopharm Co. Ltd. (Shanghai, China). All chemicals were of analytic reagent grades.

Human glioblastoma cells (U87MG cells), Brain capillary endothelial cells (bEnd.3) and Human umbilical vascular endothelial cells (HUVECs) were all obtained from Shanghai Institute of Cell Biology and maintained in Dulbecco's Modified Eagle Medium (Gibco) supplemented with 10% FBS (Gibco), 100 U/mL penicillin, and 100 μg/mL streptomycin at 37 °C under a humidified atmosphere containing 5% CO_2.

Male ICR mice and BALB/c nude mice of 4-6 weeks age were purchased from the BK Lab Animal Ltd. (Shanghai, China) and kept under SPF conditions. All animal experiments were carried out in accordance with guidelines evaluated and approved by the ethics committee of Fudan University.

2.2 Synthesis and characterization of glycopeptides and functional materials

2.2.1 Chemical synthesis of building block of N-α-(9-fluorenylmethylcarbonyl)-3-O-(2,3,4,6-tetra-O-acetyl-β-D-glucopyranosyl)-L-threonine

Scheme 2. Synthesis of N-α-(9-fluorenylmethylcarbonyl)-3-O-(2,3,4,6-tetra-O-acetyl-β-D-glucopyranosyl)-L-threonine by anomeric acetate activation method.

The lewis acid ($BF_3 \cdot Et_2O$, 10 mmol) was added to a solution of pentaacetate glucose (2.3mmol) and Fmoc-threoine (2 mmol) in DCM. The mixture was stirred for 2 h and the solution was then washed with aqueous HCl (1M), dried and concentrated (Scheme 2). The crude product was purified by column chromatography and characterized by ESI-MS.

2.2.2. Synthesis and characterization of glycopeptide and fluorescein-labeled peptide

Scheme 3. Synthetic route to glycopeptide. The synthesis of ^{9}G-A7R was taken as an example. MBHA-functionalized Rink resin was used to provide the C-terminal amides upon cleavage after classical Fmoc construction of the glycopeptide. Treatment with hydrazine hydrate ($H_2NNH_2 \bullet H_2O$) in methanol (CH_3OH) was required to remove the acetates from the glycoside moiety prior to cleavage from the Rink resin.

The peptides were synthesized by solid phase peptide synthesis using Rink-amide resin (substitution = 0.54 mmol/g) according to Fmoc methodology (Scheme 3). All the solid phase reactions were carried out manually in a sintered glasstube. Peptide condensation was facilitated by using excess Fmoc amino acid (8.8 equiv.) activated with HBTU and HOBt in DMF. The coupling reaction was allowed to proceed for 1 hour in DMF. For the glycoside-bearing residues, 1.5 equiv. of the glycosylated amino acid were used due to their expense, and the coupling reaction was prolonged for 3 hours. The Fmoc deprotection was accomplished by treating the peptide-bound resin with 20 % (vol/vol) piperidine/DMF for 15 min twice. Upon completion of the synthesis, the acetate groups of the glycoside were removed with 80 % (vol/vol) hydrazine hydrate in MeOH for 1 hour twice while on the solid phase. The resin bound peptide was washed three times with DMF and three times with DCM and methanol and dried under vacuum. The resin-bound peptides were deprotected and cleaved from the solid support with a cocktail mixture (9.5 mL of TFA, 0.25 mL of Et_3SiH and 0.25 mL of H_2O, per 1.0 g of peptide resin) for 2 hour at room temperature. After cleavage was completed, the resulting solution was concentrated to an oil in vacuo and cold Et_2O was poured over the peptide solutions to precipitate the samples. Purification of cross-linked compounds was achieved by high performance liquid chromatography (HPLC; Waters) on a reversed-phase C18 column (Waters) to yield the pure compounds. Chemical composition of the pure products was confirmed by HPLC and ESI-MS. The analytical HPLC chromatogram and mass spectral data of glycopeptide provided confirmation of purity and structural integrity.

In order to investigate the effect of modification site and number of glucose moieties, a series of threonine-based glycosylated analogues of A7R were designed. The peptides are:

(1) A7R: amino acid sequence is $^{7}A^{6}T^{5}W^{4}L^{3}P^{2}P^{1}R$; A N-terminus cysteine could be added otherwise for conjugation of fluorescein and the peptide was denoted as A7R-Cys.
(2) ^{6}G-A7R: The threonine of A7R was substituted by glycosylated threonine (Glu-Thr for short).
(3) ^{9}G-A7R: Glu-Thr was coupled at the N-terminal of A7R-Cys;
(4) ^{9,10}G-A7R: Two Glu-Thrs were coupled sequentially at the N-terminal of A7R-Cys;

Fluorescein-labeled peptide was synthesized through sulfhydryl-maleimide covalently conjugation. Briefly, 5 mg A7R-Cys was dissolved in phosphate buffer (0.1 M, pH = 7.2), 1 mg fluorescein-5-maleimide in DMF was added and gently stirred for 2 h at room temperature in the dark. The near-infrared fluorescent probe Cy7-labeled peptide was synthesized in a similar method. Fluorescein-labeled Glu-Thr was synthesized similarly to the solid phase peptide synthesis. Briefly, 1.5 equiv. of N-α-(9-fluorenylmethylcarbonyl)-3-O-(2,3,4,6-tetra-O-acetyl-β-D-glucopyranosyl)-L-threonin was coupled to Fmoc rink-amide resin. After Fmoc deprotection, 1.2 equiv. of FITC was covalently conjugated in a mixture of pyridine, DMF and DCM (12:7:5) for 1 h. The product was cleaved from resin after acetate groups deprotection and precipitate in cold n-hexane.

The target product was purified via preparative C18 reverse-phase HPLC. Pure product was ascertained by HPLC and ESI-MS.

2.2.3 Synthesis and characterization of functional materials

The targeting material A7R-PEG_{3400}-DSPE and ^{9}G-A7R-PEG_{3400}-DSPE were synthesized through covalent conjugation between thiolated peptide and mal-PEG_{3400}-DSPE. Mal-PEG_{3400}-DSPE dissolved in DMF was added to A7R-Cys or ^{9}G-A7R dissolved in phosphate buffer (0.1 M phosphate, pH 7.4) and the reaction was monitored by HPLC.

FITC-PEG_{3400}-DSPE was synthesized through covalent conjugation by stirring FITC and NH_2-PEG_{3400}-DSPE dissolved in DMF for 2 h. A ninhydrin test was adopted to confirm that no free amino group existed, which indicated that all of the DSPE-PEG_{3400}-NH_2 was linked with FITC.

The excessive peptide or FITC was removed via dialysis (MWCO 3.5 kDa) against distilled water for 48 h. The pure functional materials were obtained after lyophilization and characterized by ^{1}H-NMR (Varian 400 MHz, Palo Alto, USA).

2.3 Preparation and characterization of nanodisks

The thin-film hydration method was used to prepare the nanodisks. A mixture of the desired materials was dissolved in the chloroform, and the organic solvent was removed by rotary evaporation to form a thin film. The lipid film was dried under vacuum overnight and hydrated in phosphate buffered saline (10 mM phosphate, 150 mM NaCl, pH 7.4). Nanodisks were prepared by sonication of the hydrated solution for 45 min in an ice-bath using a JY92-II sonicator (Scientz, Ningbo, China). The resulting solution was filtered using a 0.22 μm filter to remove metal debris.

The PEG-stabilized nanodisk without modification (Disk) was composed of POPC/cholesterol/ $mPEG_{2000}$-DSPE (35:40:25, mol%). The A7R peptide or glycopeptide modified nanodisks (A7R-Disk or ^{9}G-A7R-Disk) was composed of POPC/cholesterol/$mPEG_{2000}$-DSPE/A7R-PEG_{3400}-DSPE (35:40:23:2, mol%) or POPC/cholesterol/$mPEG_{2000}$-DSPE/^{9}G-A7R-PEG_{3400}-DSPE (35:40:23:2,mol%). For FITC-labeled nanodisk, the components and ratios were POPC/cholesterol/$mPEG_{2000}$-DSPE/FITC-PEG_{3400}-DSPE (35:40:23:2, mol%) for Disk-FITC, POPC/cholesterol/$mPEG_{2000}$-DSPE/A7R-PEG_{3400}-DSPE/FITC-PEG_{3400}-DSPE (35:40:21:2:2, mol%) for A7R-Disk-FITC and POPC/cholesterol/$mPEG_{2000}$-DSPE/^{9}G-A7R-PEG_{3400}-DSPE/FITC-PEG_{3400}-DSPE (35:40:21:2:2, mol%) for ^{9}G-A7R-Disk-FITC.

For drug or fluorescein loading, PTX, Did or Dir was dissolved in the organic solvent

together with the membrane materials, which was then hydrated with PBS and sonicated. The unloaded PTX, Did or Dir was removed using a 0.1 μm filter membrane.

Cryogenic transmission electron microscope (Cryo-TEM) investigations were performed using a FEI Tecnai G20 Transmission Electron Microscope (FEI, Hillsboro, USA). The Cryo-TEM specimens were prepared by the following steps. A small drop of the Disk/PTX, A7R-Disk/PTX or ^{9}G-Disk/PTX was applied on Quantifoil grids, blotted for 4.5 s in a 100% humidity chamber, and plugged into liquid ethane (cooled by liquid nitrogen) in an FEI Vitrobot Mark IV vitrification robot. Samples were kept below -165 °C and protected from atmospheric conditions during both transfer from the preparation chamber to the microscope and during examination.

2.4 Serum stability of peptide and nanodisk

All the peptides were dissolved in phosphate buffered saline (PBS) (1 mg/mL). One hundred microliter of each peptide was incubated with 0.9 mL 25% sterile rat serum. After 0.25, 0.5, 1, 2, 4, 8, 12 and 24 h of incubation at 37°C, 20 μL of trichloroacetic acid was added into 100 μL reaction mixture. The mixture was stored at 4°C for 20 min, and then centrifuged at 12000 rpm for 10 min. Twenty microliter supernatant was analyzed by RP-HPLC to monitor and quantify peptide hydrolysis.

Nanodisks were suspended in 50% mouse serum and measurements were performed in triplicate at room temperature for 2 days. Size (diameter, nm) of nanodisk were measured at intervals by dynamic light scattering using a Zen 3600 Zetasizer (Malvern).

2.5 *In vitro* PTX release of nanodisks

Dialysis bags (MWCO 14 kDa, Millipore) with 200 μL of Disk/PTX, A7R-Disk/PTX or ^{9}G-Disk/PTX were directly immersed into 10 mL of PBS (pH 7.4) plus with 50% mouse serum. One milliliter aliquots were withdrawn from the solution periodically. The volume of solution was held constant by adding up to 10 mL after each sampling. The amount of PTX released from nanodisks was measured by absorbance at 227 nm using HPLC. The cumulative drug release was calculated from the following relationship: cumulative drug release (%) $=(M_t/M_0) \times 100\%$, where M_t is the amount of drug released from lipid disks at time t, and M_0 is the amount of drug loaded into the lipid disks.

2.6 *In vitro* cellular uptake and subcellular localization

To evaluate the targeting effect in brain microvascular endothelial cells and glioma cells. bEND.3 cells and U87 cells were incubated with 5 μM fluorescein-labeled peptide solution or various FITC-labeled nanodisk formulations for 4 h at 37 °C. The cells were stained by DAPI and visualized using a laser scanning confocal microscope (TCS SP5, Leica, Germany). To further determine the *in vitro* targeting ability and stability in serum of the nanodisks, U87 cells were incubated with FITC-labeled nanodisks (containing 5 μM of FITC) of different formulations pre-incubated with 50% mouse serum. The fluorescein-positive cells were qualitatively measured by a flow cytometer (FACS Aria; BD).

In order to investigate the cellular uptake mechanism of ^{9}G-A7R, bEND.3 and U87 cells were incubated with excess D-glucose (4.5 g/l) or A7R (100 μM) and 5 μM fluorescein-labeled peptide solution at 37°C or 4 °C for 1 h. Then the cells were stained by DAPI for imaging or gently suspended in PBS for quantitative analysis by flow cytometry.

Intracellular distribution of nanodisks was observed by co-localization as determined by confocal microscopy. bEND.3 cells and U87 cells were treated with A7R-Disk/FITC or ^{9}G-A7R Disk/FITC for 4 h at 37 °C. Cells were incubated with 50 nM LysoTracker Red (60 min) and 10 mM DAPI (10 min) to visualize lysosomes and nuclei, respectively. Then, the loading solution was removed and the cell monolayers were washed three times with ice-cold PBS, and observed with a laser scanning confocal microscope (TCS SP5, Leica, Germany).

2.7 Transport across BCECs monolayer

The BBB model was established as previously reported.[22] Rat primary brain capillary endothelial cells were isolated and seeded onto rat tail collagen coated transwell chamber. Transendothelial electrical resistance (TEER) was detected by an epithelial volt-Ωm (Millicel-RES, Millipore, USA) to evaluate cell monolayer integrity. Monolayers with TEER over 250 Ω·cm^2 were used for further experiments.

The culture medium in each apical chamber was replaced by 50 μM fluorescein-labeled peptides in glucose-free DMEM with 10% FBS. For competition assay, cells were pre-incubated for 30 min with excess glucose (4.5 g/l). After 0.5, 1, 1.5, 2, 3 and 4 h incubation at 37 °C, fluorescence intensity of the solutions collected from lower compartment was detected by a fluorescence detector (PowerWave XS, Bio-TEK, USA). At the end, the TEER was measured again to verify the integrity of the BBB model.

2.8 Targeting ability on U87MG tumor spheroids and U87 tumor spheroid/BBB co-culture model

U87 tumor spheroids were cultured by seeding U87 cells onto 2% agarose-coated 48-well plates at a density of 4 × 10^3 cells/400 μL per well. After 7 days, the tumor spheroids were incubated with different nanodisks formulations containing 5 μM FITC in DMEM with 10% FBS for 4 h. To evaluate the targeting ability in U87 tumor spheroid/BBB co-culture model, tumor spheroids were moved to the lower chamber of BBB model, and lipid disks containing 50 μM FITC were added in each apical chamber for 4 h incubation. Tumor spheroids were rinsed with PBS and fixed by 4% paraformaldehyde for 30 min then imaged by a confocal laser microscopy.

2.9 *In vivo* brain and glioma targeting

To compare the brain targeting efficiency of different glycopeptide, male ICR mice 4~6 weeks of age were injected with 100 μL Cy7-labeled peptide phosphate buffer via tail vein. One hour after injection, mice were sacrificed and the brains were dissected for *ex vivo* fluorescence imaging using an *in vivo* imaging system (IVIS Spectrum, Caliper, USA).

To evaluate the relative tumor targeting efficiency of ^{9}G-A7R, the subcutaneous xenograft tumor models were established by inoculation of 4 × 10^6 U87MG cells (cells suspended in 100 μl PBS) into the subcutaneous tissue of the right subaxillary of male Balb/c nude mice. After two weeks when the tumor volume was about 200 mm^3, the mice were injected with 100 μL of Cy7-labeled peptide phosphate buffer. After 1 h of injection, mice were sacrificed and the tumors were dissected for *ex vivo* fluorescence imaging.

To further investigate the intracranial glioma targeting efficiency of ^{9}G-A7R, the U87MG glioma mouse model was prepared by inoculation of 6 × 10^5 cells in 5 μl PBS into the right striatum (1.8 mm lateral, 0.6 mm anterior to the bregma and 3 mm of depth) of male Balb/c nude mice. After 7 days of implantation, the intracranial U87MG tumor bearing mice were injected with

100 μL of Cy7-labeled peptide phosphate buffer. After 1 h post-injection, the fluorescent images were detected using an *in vivo* image system, therefore tissues were harvested and imaged.

Glioma targeting ability of nanodisks of different formulations was also investigated in a similar way, the model mice were respectively administrated with 100 μL of DiR encapsulated nanodisks of different formulations via tail vein 7 days post-implantation. The fluorescence images were acquired at predetermined time points and the brains were dissected for *ex vivo* imaging 12 h after injection by the IVIS imaging system (IVIS Spectrum, Caliper, USA). Immunofluorescence assay was performed by injecting FITC-labeled nanodisks into the model mice 7 days post-implantation. After 4 h, the brains were harvested and frozen in Tissue Tek O.C.T. compound after dehydration. Then, the brains were cut into 10 μm thick sections and stained with 300 nM DAPI and anti-CD31 antibody. The sections were examined under a confocal laser scanning microscope.

2.10 Hemodynamics of the nanodisks

The kinetic properties of nanodisks with different formulations were analyzed in ICR mice. Mice were injected with 100 μL DiD-loaded nanodisks via tail vein. At the time points of 1, 5, 10, 15, 30 min and 1, 2, 4, 8, 12, 24, 48, 72 h post injection, 50 μL blood was sampled from the retro-orbital sinus. The blood samples were diluted 4 times for fluorescence quantification by a microplate reader (Power Wave XS, Bio-TEK, USA). The pharmacokinetic parameters of the nanodisks were analyzed by DAS2.0.

2.11Biodistribution of nanodisks in intracranial U87 xenograft bearing mice

Nude mice bearing intracranial U87 xenograft were injected with 100 μL DiD-loaded lipid disks via tail vein. Twelve hours after injection, blood and homogenate of main organs and tumor tissues (peeled off from the brain) were collected for fluorescence analysis by a microplate reader (Power Wave XS, Bio-TEK, USA).

2.12 Cytotoxicity assay

The *in vitro* cytotoxicity of PTX-loaded nanodisks was determined using MTT assay. U87 cells were seeded into 96-well culture plates at a density of 4×10^3 cells/100 μL per well. After 24 h cultivation at 37 °C, the cells were treated with different concentrations of PTX-loaded nanodisks formulations. The cytotoxicity was determined at 72 h by MTT assay.

2.13Inhibition of tube formation *in vitro*

Matrigel basement was added into a 24-well plate and incubated at 37 °C for 30 min. Then U87 cells or HUVEC resuspended with DMEM medium containing 100 ng/mL of PTX-loaded nanodisks were seeded onto the pre-coated matrigel basement plate. The plate was incubated overnight and then observed and photographed under an inverted phase contrast microscope (DMI4000 B, Leica, Germany). The cells treated with blank DMEM medium were set as the control group. The amount of tubes was counted within three randomly visions and collected for statistically analysis.

2.14Anti-tumor effect in intracranial U87 xenograft -bearing nude mice

Nude mice bearing intracranial U87 xenograft were used for the anti-tumor studies. The mice were randomly divided into five groups (n=8) and treated with saline, Taxol, Disk/PTX, A7R-Disk/PTX and ^{9}G-A7R-Disk/PTX via tail vein on the day 5, 7, 9, 11 and 13 after implantation with a total PTX dose of 25 mg/kg. The survival times were recorded. One day after the final treatment, mice were sacrificed and brains with tumor were obtained for

immuno-histochemical analysis. The brains were fixed with 4% paraformaldehyde, paraffin-embedded and sectioned. TUNEL assay was conducted to detect the apoptotic cells. CD31/PAS dual staining was conducted to observe the microvessels. TUNEL-positive cells or CD31-positive cells in three slices were counted.

2.15 Statistical analysis

Data were plotted as mean ± SD unless otherwise indicated. Comparison among the different groups was measured by the one-way ANOVA with Bonferroni correction. $p<0.05$was considered statistically significant.

3. Results

3.1 Characterization of glycopeptide

The threonine-based glycosylated analogues of A7R were synthesized via the Fmoc-protected solid phase peptide synthesis method. The first step was the synthesis of building block, i.e. glycosylated threonine residue (Glu-Thr). The crude peptide was purified and analyzed by HPLC and the molecular mass were ascertained by ESI-MS (Fig. 1 and Fig. S1). The *m/z*$[M+H]^+$ of Glu-Thr, A7R, ^{6}G-A7R, ^{9}G-A7R and ^{9,10}G-A7R were respective 672.6 Da, 943.4 Da, 1104.4 Da, 1205.4 Da and 1467.4 Da. The determined molecular mass was within experimental errors of the expected values, indicating the successful synthesis of a series of glycopeptides. Fluorescein-labeled and Cy7-labeled peptides were also characterized by HPLC and ESI-MS (data not shown).

Figure 1. Analysis and characterization of glycopeptide. HPLC and ESI-MS of A7R-Cys (A) and ^{9}G-A7R (B). The conditions of HPLC analysis were as follows: temperature: 40 °C; C18 column: YMC, 3.5 μm, 4.6×150 mm; running phase: 5-65% acetonitrile in water with 0.1% TFA; flow rate: 0.7 mL/min.

3.2 Comparison and screening of glycopeptide

A7R was shown to bind specifically to VEGFR2 and NRP-1 overexpressed on glioma. Amino-acid deletion analysis revealed that four C-terminal residues (LPPR) and particularly the C-terminal arginine with a free carboxyl group were essential for A7R activity[23]. The effect of modification site and number of glucose moieties on A7R bioactivity were investigate. A series of threonine-based glycosylated analogues of A7R were designed, including ^{6}G-A7R with the glucose moiety at the side chain, ^{9}G-A7R with the glucose moiety at the N-termini and ^{9,10}G-A7R with the two glucose moieties at the N-termini. C-terminal modification was not conducted.

The stability of glycopeptides was studied by incubating with fresh rat serum and the intact peptide after incubation was determined by RP-HPLC. As shown in Fig. 2A, A7R and ^{6}G-A7R degraded quickly in serum and almost vanished after 2 h incubation. In contrast, ^{9}G-A7R and ^{9,10}G-A7R were much more stable in serum than A7R. Fifty percent of glycopeptides remained intact after 2 h incubation.

To investigate the effect of glycosylation on cellular uptake by glioma cells，fluorescently labeled peptides were incubated with U87 cells and the uptake by U87 cells were quantitated by flow cytometry. As shown in Fig. 2B, both A7R (77.7%) and glycosylated threonine residue (Thr-Glu-Flu) (70%) showed high uptake efficiency by U87 cells. ^{9}G-A7R and ^{9,10}G-A7R exhibited slightly enhanced or similar uptake efficiency of 82.2% and 75.2% compared with A7R, respectively. However, ^{6}G-A7R exhibited weaken uptake efficiency of 49.8%.

To investigate the GLUT-meditated brain transport, uptake of peptides by bEND.3 cells was analyzed by flow cytometry (Fig 2C). A7R could barely be taken up by bEND.3 cells, while glycosylation at the N-termini of A7R, such as ^{9}G-A7R and ^{9,10}G-A7R, effectively facilitated uptake by bEND.3 cells. ^{6}G-A7R could not target brain capillary endothelial cells because the glucose residue would hardly reach the deep binding pocket of GLUT1[9]. Cy7 was employed as a fluorescent dye to further compare the brain distribution between A7R and glycopeptide *in vivo*. One hour after injection, mice were sacrificed and the brains were dissected for imaging. The fluorescence intensity of A7R-Cy7 and ^{6}G-A7R in the brain was negligible, indicating that they barely crossed the BBB *in vivo* (Fig. 2D). ^{9}G-A7R and ^{9,10}G-A7R could accumulate effectively in the brain according to the semi-quantitative analysis of fluorescence intensity (Fig. 2E). However, there was no significant difference between ^{9}G-A7R and ^{9,10}G-A7R, indicating more glucose moieties did not significantly improve the brain transport of peptide. These findings were consistent with the results of *in vitro* cellular uptake by bEND.3 cells.

Based on the aforementioned results, ^{9}G-A7R and ^{9,10}G-A7R showed advantages over A7R and ^{6}G-A7R. ^{9}G-A7R was selected as for further studies for its ease of synthesis and high targeting efficiency.

Figure 2. Performance of glycopeptides. (A) Stability of peptide in 25% rat serum at 37 ℃ determined by HPLC. U87 (B) and bEND.3 cells (C) uptake of a series of glycopeptides analyzed by flow cytometry. (D) *Ex vivo* near-infrared imaging of harvested brains 1 h post injection. (E) Semi-quantitative analysis of the mean fluorescence intensity of the dissected brains (mean ± SD, n = 3). ***$p < 0.001$, **$p < 0.01$.

3.3 Brain and glioma targeting ability of ^{9}G-A7R *in vitro* and *in vivo*

3.3.1 Brain targeting ability of ^{9}G-A7R on BBB model

The *in vitro* BCECs monolayer was established to evaluate the brain targeting ability of ^{9}G-A7R peptide. The cell monolayer with qualified transendothelial electrical resistance (TEER > 250 Ω•cm^{2}) was characterized for further experiments. The transport ratios for all groups increased in a time-dependent manner (Fig. 3A). After 4 h, 1.16 ± 0.36 % of ^{9}G-A7R traversed the BBB, which was greater than that of A7R (0.61 ± 0.22%). A7R displayed lower efficiency at all tested time points in comparison to ^{9}G-A7R. For competition assay, excess D-glucose was pre-incubated with BCECs monolayers for 30 min to saturate GLUT1 at the luminal side, followed by incubation with fluorescein labeled ^{9}G-A7R. Transport of ^{9}G-A7R was dramatically undermined with D-glucose pretreatment, confirming that the glucose transporter was involved in the transport of ^{9}G-A7R across the BBB.

3.3.2 Cellular uptake mechanism of ^{9}G-A7R by bEND.3 cells and U87 cells

Glycopeptide is composed mainly of two parts: glucose moieties and A7R peptide. Fig. S2 illustrated cellular uptake and competition inhibition effect on the uptake by bNED.3 and U87 cells. The cellular uptake of ^{9}G-A7R by bNED.3 cells was energy independent and could be inhibited by glucose not A7R (Fig. S2A). However, uptake of ^{9}G-A7R by U87 cells showed some discrepancies. Fig. S2B showed that the cellular uptake by U87 cells was energy independent and could be inhibited by A7R not glucose. In contrast, glucose might provide energy to promote uptake of ^{9}G-A7R by U87 cells. The data suggested that glycosylation indeed enabled A7R across the BBB through the GLUT1.

3.3.3 Tumor targeting ability in intracranial and subcutaneous U87 xenograft bearing nude mice

The glioma targeting ability of ^{9}G-A7R with the existence of BBB were tested in intracranial U87 xenograft bearing nude mice. Peptide was labled with near-infrared dye Cy7 for *ex vivo* imaging. As shown in Fig. 3B and C, free A7R rarely distributed in the brain or brain tumor. The fluorescence was higher in the tumor region after the treatment of ^{9}G-A7R, suggesting of effective and precise targeting for glioma.

To further verify the relative tumor targeting ability of ^{9}G-A7R without the existence of BBB, we also established subcutaneous U87 model. One hour after i.v. administration, main organs and tumor tissues were dissected for *ex vivo* imaging. As shown in Fig. 3D and E, ^{9}G-A7R displayed higher accumulation in glioma in comparison to A7R. The average fluorescence intensity of ^{9}G-A7R-Cy7 group was about 4.7 times higher than that of A7R-Cy7 group in tumor tissues.

Figure 3. Brain and tumor targeting ability of ^{9}G-A7R *in vitro and in vivo*. (A) Transmembrane transport efficiency of A7R and ^{9}G-A7R in the *in vitro* BBB monolayer. *Ex vivo* near-infrared imaging (B) and semi-quantitative analysis of the mean fluorescence intensity from the Cy7-labeled peptide (C) of harvested brains 1 h post-injection in intracranial U87 xenograft bearing nude mice. *Ex vivo* near-infrared imaging (D) and semi-quantitative analysis of the mean fluorescence intensity from the Cy7-labeled peptide (E) of disserted organs 1 h post-injection in subcutaneous U87 xenograft bearing nude mice. (Mean ± SD, n = 3). $^{**}p < 0.01$, $^{***}p < 0.001$.

3.4 Characterization of PTX-loaded lipid-nano disk

The functional materials A7R-PEG$_{3400}$-DSPE and ^{9}G-A7R-PEG$_{3400}$-DSPE were synthesized using a sulfhydryl-maleimide coupling method. The purified materials were characterized by HPLC and ^{1}H-NMR analysis (Fig. S3A and B). In the ^{1}H-NMR spectrum of mal-PEG$_{3400}$-DSPE, the maleimide group exhibited a peak at 6.7 ppm, while the peak completely disappeared in the spectrum of A7R-PEG$_{3400}$-DSPE and ^{9}G-A7R-PEG$_{3400}$-DSPE, indicating a successful synthesis of the targeting materials.

Cryo-TEM enables direct visualization of the shape and particle size of nanodisks. Cryo-TEM images revealed disk-shaped structures with a diameter of approximately 50 nm (Fig. 4). A7R or glycopeptide modification did not induce obvious morphological changes. All the nanodisks exhibited good stabilities in mouse serum (Fig. S3F). All PTX-loaded nanodisk formulations displayed similar PTX release profiles as shown in Fig. S3G. The zeta potentials of Disk/PTX, A7R-Disk/PTX and ^{9}G-A7R-Disk/PTX were respective -2.71 ± 1.05 mV, -1.58± 0.41mV and -1.49± 1.16 mV. The drug loading efficiency of Disk/PTX, A7R-Disk/PTX and ^{9}G-A7R-Disk/PTX was respective 8.45 ± 0.058 %, 8.14 ± 0.12 % and 7.84 ± 0.067 % (Table S1).

Figure 4. Cryo-TEM images of Disk/PTX (C), A7R-Disk/PTX (D) and ^{9}G-A7R-Disk/PTX (E).

3.5 Brain and tumor targeting ability of nanodisk *in vitro* and *in vivo*

3.5.1 *In vitro* cellular uptake by brain capillary endothelial cells and U87 cells

Cellular uptake of various FITC-labeled nano-disk formulations by bEND.3 and U87 cells was conducted to evaluate the targeting property. As shown in Fig. 5A and C, ^{9}G-A7R-Disk could be significantly taken up by bEND.3 cells in comparison to Disk or A7R-Disk, indicating that glycopeptide modification could enhance the uptake of disks by brain capillary endothelial cells through glucose transporter 1 (GLUT1). Moreover, in the cellular uptake by U87 cells, the

intracellular fluorescence intensity in ^{9}G-A7R-Disk treated cells was significant higher than that of Disk or A7R-Disk (Fig. 5B), and it was attributed to the enhanced stability of glycopeptide[24]. As confirmed in Fig. 5D, the pre-incubation with mouse serum would not obviously impair the cellular uptake of ^{9}G-A7R-Disk while the uptake of Disk or A7R-Disk was significantly reduced.

Lysosomes were labeled with Lyso-Tracker Red to track intracellular distribution of nanodisks. It showed obvious co-localization of A7R-Disk or ^{9}G-A7R-Disk after 4 h incubation with bEND.3 or U87 cells (except that A7R-Disk could not internalized into bEND.3 cells), suggesting lysosomes were involved in the internalization of the nanodisks (Fig. 5E and F). Thus the stability of glioma targeting moiety during the BBB transcytosis process became particularly important and the glycopeptide modified nanodisks would maintain targeting ability in the harsh lysosomal environment.

Figure 5. Cellular uptake and subcellular localization of different nanodisks by bEND.3 (A, C and E) and U87 cells (B, D and F). FITC-positive cells were calculated by a flow cytometer, and intracellular fluorescence was captured by a confocal laser scanning microscope. Scale bars represent 10 μm.

3.5.2 Targeting ability of nanodisks to U87 tumor spheroids and U87 tumor spheroid/BBB co-culture model

U87MG tumor spheroids were established to assess the penetration efficiency of nanodisks. As shown in Fig. 6A, both nanodisks modified with A7R or ^{9}G-A7R showed efficient uptake, but the fluorescent intensity of tumor spheroid treated with ^{9}G-A7R-Disk was higher than that of plain Disk or A7R-Disk. In order to better mimic the situation of brain tumor, a BBB/U87 tumor spheroids co-culture model was established to assess the targeting ability of nanodisks modified with A7R and ^{9}G-A7R *in vitro*. As shown in Fig. 6B, A7R-Disk could not cross the BBB thus no tumor spheroid targeting ability, whereas only the tumor spheroid treated with ^{9}G-A7R-Disk exhibited obviously uptake.

Figure 6. Uptake of FITC-labeled Disk, A7R-Disk and ^{9}G-A7R-Disk by U87 tumor spheroids (A) and U87 tumor spheroid/BBB co-culture model (B). Tumor spheroid penetration was examined by a confocal microscope, with a 5 μm interval between consecutive slides.

3.5.3 *In vivo* brain glioma targeting effect

To assess the glioma targeting ability *in vivo*, DiR-loaded nanodisks were intravenously injected into mice bearing intracranial U87MG tumor. The results of semi-quantitative ROI analysis by the software of living image indicated that ^{9}G-A7R-Disk led to the highest accumulation in glioma, which reached peak value at 4 h post-injection (Fig. 7A and B). The images of excised brains and its semi-quantitative analysis also indicated that nanodisks modified with ^{9}G-A7R showed the strongest fluorescence accumulation in glioma, which was around 4-fold higher than that of A7R-Disk (Fig. 7C and D). Frozen brain glioma sections were obtained to visualize the precise distribution of nanoparticles within the tumor site (Fig. 7E). The ^{9}G-A7R-Disk were mostly distributed around blood vessels and taken up by glioma cells. In contrast, only weak fluorescence signal from plain Disk or A7R-Disk was observed within tumor.

Figure 7. *In vivo* targeting ability of nanodisks in intracranial U87 glioma. *In vivo* fluorescence imaging of intracranial U87MG tumor (A) and semi-quantitative ROI analysis (B) of *in vivo* fluorescent images at different time points after intravenous injection of DiR-loaded nanodisks. *Ex*

vivo near-infrared imaging of the harvested brains (C) and semi-quantitative ROI analysis of the mean fluorescence intensity in tumors (D) from the DiR-loaded nanodisks 12 h post-injection. (Mean ± SD, n =3). (E) The distribution of nanodisks in the glioma of tumor-bearing mice 7 days post-implantation. Frozen sections were examined under a fluorescence microscope. Nuclei were stained with DAPI (blue), blood vessels were labeled with anti-CD31 (red), while green represents the FITC-labeled nanodisks (scale bar=50 μm).

3.5.4 Blood dynamics and biodistribution of nanodisks

To investigate the systemic circulation time of nanodisks, DiD-loaded disks were administrated into each mouse via tail vein. Blood was sampled at different time points for fluorescence measurements. Relative plasma concentration-time curves of nanodisks after i.v. injection were presented in Fig. S4A and pharmacokinetic parameters were obtained by noncompartmental analysis. The mean residence time (MRT) of Disk was as high as 21.76 hours, however, modification with A7R or ^{9}G-A7R reduced the MRT of Disk to some extent. The biodistribution of nanodisks in intracranial U87 xenograft bearing mice was further studied. DiD-loaded disks were administrated into each mouse via tail vein and blood and homogenate of main organs were collected for fluorescence analysis 12 h post injection. As shown in Fig. S4B, all the nanodisks had very high retention in blood compared to other organs. Modification with glycopeptide of disk inevitably increased the uptake by the endothelial reticular system (RES), which explained the reduced MRT of ^{9}G-A7R-Disk. Meanwhile, the accumulation in tumor tissue was significantly enhanced using glycopeptide to cross the BBB. The results indicated that modification with glycopeptide could enable nanodisks traverse the BBB and significantly elevated glioma accumulation.

3.6 *In vitro* and *in vivo* anti-tumor effect

3.6.1 Cytotoxicity of PTX-loaded nanodisks *in vitro*

In vitro cytotoxicity of PTX-loaded nanodisks were investigated in U87 by the MTT assay (Fig. 8A). Inhibition of cell growth was studied after 72 h. The IC_{50} value of Taxol, Disk/PTX and A7R-Disk/PTX were 43.66, 74.90 and 38.85 nM, respectively, while the IC_{50} value of ^{9}G-A7R-Disk/PTX was 26.36 nM. The results indicated that the inhibitory effect to the proliferation of U87 cells was markedly elevated after the incorporation of glycopeptide.

3.6.2 *In vitro* destroying ability against U87MG VM channels and HUVEC tubes

U87 vasculogenic mimicry (VM) and HUVEC tubes were used to evaluate the inhibitive effects of PTX-loaded nanodisks (Fig. 8B-D). Cells treated with DMEM formed extensive and enclosed tube networks. Networks of cells subjected to various PTX formulations exhibited a different degree of fracture. ^{9}G-A7R-Disk exhibited higher inhibitive effects in both U87 VM tubes and HUVEC tubes than did A7R-Disk and plain Disk. These results were consistent with the results of cytotoxicity, indicating the cytotoxic effect of nanodisks was significantly enhanced by the glycopeptide modification.

Figure 8. Anti-tumor effect of PTX-loaded nanodisks *in vitro*. (A) Cytotoxicity of various PTX-loaded nanodisks against U87 cells was assessed using MTT assay after 72 h incubation (mean ± SD, n =3). The IC_{50} values were calculated using GraphPad Prism 7.0. (B) Effect of various PTX-loaded nanodisks on U87 VM formation and HUVEC tube formation. The quantitative data of the U87 VM formation (C) and HUVEC tube formation (D) treated by

different PTX-loaded nanodisks. Cells incubated with drug-free DMEM served as the control. Data are presented as the percentages of the control group, which was set at 100%. *p<0.05, **p<0.01, ***p<0.001. Bar = 200 μm.

3.6.3 Anti-tumor efficacy of *in vivo*

To evaluate the potential therapeutic efficacy of PTX-loaded nanodisks for the treatment of brain tumors, intracranial U87 xenograft bearing nude mice were used and the survival results were represented in a Kaplan-Meier plot in Fig. 9A. The median survival time of the mice treated with ^{9}G-A7R-Disk/PTX (33.5 days) was significantly longer than that of those treated with A7R-Disk/PTX (28 days), Disk/PTX (28.5 days) and Taxol (26.5 days), thus increasing the anti-glioma effect by 2.83, 2.43 and 5.67-fold, respectively. TUNEL and CD31/PAS immunohistochemical staining were conducted (Fig. 9B-D). ^{9}G-A7R-Disk/PTX treatment induced significant apoptosis and remarkably inhibited angiogenesis in tumor site in comparison to other treatments. These results indicated that nanodisks modified with glycopeptide exhibited a significant improvement in anti-tumor activities, an effect attributed to its ability across the BBB.

Figure 9. Therapeutic efficacy of PTX-loaded nanodisks *in vivo*. (A) Kaplan–Meier survival curves of nude mice bearing intracranial U87 glioma. Mice (n =8) were injected at 5, 7, 9, 11 and 13 days after glioma implantation with saline, Taxol, Disk/PTX, A7R-Disk/PTX and ^{9}G-A7R-Disk/PTX. (B) CD31/PAS dual staining analysis and TUNEL immunohistochemical staining of tumor sections after various treatments. Quantification of the percentage of TUNEL positive apoptotic cells (C) and angiogenesis inhibition (D) in tumor treated with different disk formulations in comparison to saline group. *p<0.05, **p<0.01. Scale bar =100 μm.

4. Discussion

Heptapeptide ATWLPPR (A7R) binds specifically to VEGFR2 and NRP-1 which holds promise in tumor imaging[25.26] and active drug delivery[27-29]. Our previous studies have demonstrated that A7R-modified liposomes exhibited excellent glioma-targeting ability in subcutaneous tumor model[28.29]. Considering the BBB and enzymatic degradation of peptide in treatments of glioma *in vivo*, strategy of glycosylation was applied to make A7R versatile.

Amino-acid deletion analysis revealed that four C-terminal residues (LPPR) and particularly the C-terminal arginine with a free carboxyl group were essential for A7R activity[23]. Therefore the effect of modification site and number of glucose moieties was investigated. We compared the serum stability, the intrinsic targeting activity of glioma cells and uptake ability of brain endothelial cells among the analogues of A7R. For serum stability, our results showed that A7R and ^{6}G-A7R (imitating natural O-linked glycopeptide with the glucose moieties on the side chain of A7R) were degraded quickly in rat serum. By contrast, N-terminal glycopeptide (^{9}G-A7R and ^{9,10}G-A7R) exhibited enhanced stability (Fig. 2A). For the uptake of U87 cells, ^{9}G-A7R and ^{9,10}G-A7R had high uptake efficiency as A7R while ^{6}G-A7R showed some decrease (Fig. 2B). We speculate that the glucose moieties in ^{6}G-A7R were so close to the C-terminal residuals to impede the binding of A7R to the receptor. For the comparison of brain targeting ability, the N-terminal glycopeptide (^{9}G-A7R and ^{9,10}G-A7R) showed a similar superior effect to A7R and ^{6}G-A7R *in vitro* and *in vivo* (Fig. 2C and D). Based on the experimental results above, ^{9}G-A7R was selected as the optimal one for further study considering its simplicity and validity.

It is noteworthy that tumor cells deviate from most normal tissues and exhibit a dysfunctional and ravenous consumption of glucose, known as Warburg effect[30]. GLUT1 is also found to be

overexpressed on brain tumor cells, thus can be utilized for tumor targeting[11.31]. However, the glucose ligand did not increase the uptake of ^{9}G-A7R by U87 cells through GLUT1 (Fig. S3B), the increased accumulation in tumor tissues might result from enhanced serum stability. For brain glioma targeting, ^{9}G-A7R was proved to exhibit a two-stage targeting process. Firstly ^{9}G-A7R tranversed the BBB through GLUT-mediated transport and afterwards targeted the brain glioma through receptor-mediated transcytosis.

A7R has been reported to decrease the tumor angiogenesis and growth at a relative high dosage[32]. However, in our studies, neither high doses of A7R nor ^{9}G-A7R could significantly prolong the median survival time of glioma-bearing mice (Fig. S5). In contrast, the advantage of ^{9}G-A7R is in line with its glioma targeting ability rather than therapeutic effect. Thus, it is of great potential to use ^{9}G-A7R as the targeting ligand in drug delivery system.

In order to enable A7R to cross the BBB, we performed glycosylation strategy, which would inevitably increase the accumulation in reticuloendothelial system (RES) due to the introduction of glucose molecule. However, biodistribution results in subcutaneous tumor mice suggest that glycopeptide molecule has the most significant targeting effect at the tumor site, 4.7 fold more potent than A7R. The relative targeting in the tumor site was much higher than that in other organs. Modification of glycopeptides on the surface of nano-lipid nanodisks also significantly increased the accumulation in brain tumor sites. It is noteworthy that, compared with other organs, the nanodisk exhibited very high content in the blood, suggesting a long blood circulation capacity. The hydrophobic core of the lipid disk provided a reservoir for the insoluble small molecule drug. The PTX-loaded nanodisk has a good tumor killing effect and can significantly prolong the survival of glioma-bearing mice.

5. Conclusions

In summary, a functional glycopeptide ^{9}G-A7R was developed to overcome enzymatic and BBB barriers by employing glycosylation strategy. ^{9}G-A7R was resistant to serum enzymes and could penetrate the BBB through GLUT-mediated transcytosis and afterwards target the brain glioma through receptor-mediated endocytosis. A novel glioma-targeted drug delivery system was constructed successfully employing ^{9}G-A7R as the targeting moiety and nanodisk as the carrier of paclitaxel. The delivery system could precisely target glioma in nude mouse xenograft models and exhibit superior anti-glioma efficacy. The glycopetide modified nanodisk showed a promising application for brain glioma therapy.

Acknowledgements

This work was supported by National Natural Science Foundation of China (81773657, 81690263 and 81473149), Shanghai Education Commission Major Project (2017-01-07-00-07-E00052) and Shanghai International Science and Technology Cooperation Project (16430723800)

References:

[1] K. Anjum, B.I. Shagufta, S.Q. Abbas, S. Patel, I. Khan, S.A.A. Shah, N. Akhter, S.S.U. Hassan, Current status and future therapeutic perspectives of glioblastoma multiforme (GBM) therapy: A review, Biomed. Pharmacother. 92(2017) 681-689.

[2] M. Reni, E. Mazza, S. Zanon, G. Gatta, C.J. Vecht, Central nervous system gliomas, Critical Reviews in Oncology/Hematology 113(2017) 213-234.

[3] K.A. Ghotme, G.E. Barreto, V. Echeverria, J. Gonzalez, R.H. Bustos, M. Sanchez, J. Leszek, N.S. Yarla, R.M. Gomez, V.V. Tarasov, G.M. Ashraf, G. Aliev, Gliomas: New Perspectives in Diagnosis, Treatment and Prognosis, Curr. Top. Med. Chem. 17(2017) 1438-1447.

[4] M.V. Wanjale, G. Kumar, Peptides as a therapeutic avenue for nanocarrier-aided targeting of glioma, Expert Opin. Drug Deliv. 14(2017) 811-824.

[5] A.S. Wadajkar, J.G. Dancy, D.S. Hersh, P. Anastasiadis, N.L. Tran, G.F. Woodworth, J.A. Winkles, A.J. Kim, Tumor-targeted nanotherapeutics: overcoming treatment barriers for glioblastoma, Wiley Interdiscip. Rev. Nanomed. Nanobiotechnol. 9(2017).

[6] L. Lu, H. Qi, J. Zhu, W.X. Sun, B. Zhang, C.Y. Tang, Q. Cheng, Vascular-homing peptides for cancer therapy, Biomed. Pharmacother. 92(2017) 187-195.

[7] A. David, Peptide ligand-modified nanomedicines for targeting cells at the tumor microenvironment, Adv. Drug Deliv. Rev. 119(2017) 120-142.

[8] M. Ying, Q. Shen, C. Zhan, X. Wei, J. Gao, C. Xie, B. Yao, W. Lu, A stabilized peptide ligand for multifunctional glioma targeted drug delivery, J. Control. Release 243(2016) 86-98.

[9] D. Deng, C. Xu, P. Sun, J. Wu, C. Yan, M. Hu, N. Yan, Crystal structure of the human glucose transporter GLUT1, Nature 510(2014) 121-125.

[10] X. Fu, G. Zhang, R. Liu, J. Wei, D. Zhang-Negrerie, X. Jian, Q. Gao, Mechanistic Study of Human Glucose Transport Mediated by GLUT1, J. Chem. Inf. Model. 56(2016) 517-526.

[11] X. Jiang, H. Xin, Q. Ren, J. Gu, L. Zhu, F. Du, C. Feng, Y. Xie, X. Sha, X. Fang, Nanoparticles of 2-deoxy-d-glucose functionalized poly(ethylene glycol)-co-poly(trimethylene carbonate) for dual-targeted drug delivery in glioma treatment, Biomaterials 35(2014) 518-529.

[12] C. Zhang, W. Zhao, L. Liu, R. Ju, L. Mu, Y. Zhao, F. Zeng, H. Xie, Y. Yan, W. Lu, A nanostructure of functional targeting epirubicin liposomes dually modified with aminophenyl glucose and cyclic pentapeptide used for brain glioblastoma treatment, Oncotarget 6(2015) 32681.

[13] I. Harbi, B. Aljaeid, K.M. El-Say, A.S. Zidan, Glycosylated Sertraline-Loaded Liposomes for Brain Targeting: QbD Study of Formulation Variabilities and Brain Transport, AAPS Pharmscitech 17(2016) 1404-1420.

[14] X. Wei, C. Zhan, Q. Shen, W. Fu, C. Xie, J. Gao, C. Peng, P. Zheng, W. Lu, AD -Peptide Ligand of Nicotine Acetylcholine Receptors for Brain-Targeted Drug Delivery, Angew. Chem. Int. Ed. 54(2015) 3023-3027.

[15] B.D. Green, M.H. Mooney, V.A. Gault, N. Irwin, C.J. Bailey, P. Harriott, B. Greer, F. O'Harte, P.R. Flatt, N-terminal His(7)-modification of glucagon-like peptide-1(7-36) amide generates dipeptidyl peptidase IV-stable analogues with potent antihyperglycaemic activity, J. Endocrinol. 180(2004) 379-388.

[16] N.O. Elmagbari, Antinociceptive Structure-Activity Studies with Enkephalin-Based Opioid

Glycopeptides, J. Pharmacol. Exp. Ther. 311(2004) 290-297.

[17] B.D. Green, V.A. Gault, F.P. O'Harte, P.R. Flatt, A comparison of the cellular and biological properties of DPP-IV-resistant N-glucitol analogues of glucagon-like peptide-1 and glucose-dependent insulinotropic polypeptide, Diabetes Obes. Metab. 7(2005) 595-604.

[18] T. Ueda, K. Tomita, Y. Notsu, T. Ito, M. Fumoto, T. Takakura, H. Nagatome, A. Takimoto, S. Mihara, H. Togame, K. Kawamoto, T. Iwasaki, K. Asakura, T. Oshima, K. Hanasaki, S. Nishimura, H. Kondo, Chemoenzymatic synthesis of glycosylated glucagon-like peptide 1: effect of glycosylation on proteolytic resistance and in vivo blood glucose-lowering activity, J. Am. Chem. Soc. 131(2009) 6237-6245.

[19] J. Gao, C. Xie, M. Zhang, X. Wei, Z. Yan, Y. Ren, M. Ying, W. Lu, RGD-modified lipid disks as drug carriers for tumor targeted drug delivery, Nanoscale 8(2016) 7209-7216.

[20] E. Johansson, C. Engvall, M. Arfvidsson, P. Lundahl, K. Edwards, Development and initial evaluation of PEG-stabilized bilayer disks as novel model membranes, Biophys. Chem. 113(2005) 183-192.

[21] W. Zhang, J. Sun, Y. Liu, M. Tao, X. Ai, X. Su, C. Cai, Y. Tang, Z. Feng, X. Yan, G. Chen, Z. He, PEG-Stabilized Bilayer Nanodisks As Carriers for Doxorubicin Delivery, Mol. Pharmaceut. 11(2014) 3279-3290.

[22] P. Zhang, L. Hu, Y. Wang, J. Wang, L. Feng, Y. Li, Poly(epsilon-caprolactone)-block-poly(ethyl ethylene phosphate) micelles for brain-targeting drug delivery: in vitro and in vivo valuation, Pharm. Res. 27(2010) 2657-2669.

[23] P.L.R.V. Anna Starzec, C.H.D.P. Alda Navaza, Structure-function analysis of the antiangiogenic ATWLPPR peptide inhibiting VEGF165 binding to neuropilin-1 and molecular dynamics simulations of the ATWLPPR/neuropilin-1 complex, Peptides 28(2007) 2397-2402.

[24] M. Ying, Q. Shen, Y. Liu, Z. Yan, X. Wei, C. Zhan, J. Gao, C. Xie, B. Yao, W. Lu, Stabilized Heptapeptide A7R for Enhanced Multifunctional Liposome-Based Tumor-Targeted Drug Delivery, ACS Appl. Mater. Inter. 8(2016) 13232-13241.

[25] L. Mey, M. Hormann, N. Schleicher, P. Reuter, S. Donges, R. Kinscherf, M. Gassmann, T. Gerriets, N. Al-Fakhri, Neuropilin-1 modulates vascular endothelial growth factor-induced poly(ADP-ribose)-polymerase leading to reduced cerebrovascular apoptosis, Neurobiol. Dis. 59(2013) 111-125.

[26] H. Wu, H. Chen, D. Pan, Y. Ma, S. Liang, Y. Wan, Y. Fang, Imaging integrin alphavbeta 3 and NRP-1 positive gliomas with a novel fluorine-18 labeled RGD-ATWLPPR heterodimeric peptide probe, Mol. Imaging Biol. 16(2014) 781-792.

[27] H. Slimani, E. Guenin, D. Briane, R. Coudert, N. Charnaux, A. Starzec, R. Vassy, M. Lecouvey, Y.G. Perret, A. Cao, Lipopeptide-based liposomes for DNA delivery into cells expressing neuropilin-1, J. Drug Target. 14(2006) 694-706.

[28] M. Ying, Q. Shen, Y. Liu, Z. Yan, X. Wei, C. Zhan, J. Gao, C. Xie, B. Yao, W. Lu, Stabilized Heptapeptide A7R for Enhanced Multifunctional Liposome-Based Tumor-Targeted Drug Delivery, ACS Appl. Mater. Inter. 8(2016) 13232-13241.

[29] M. Ying, C. Zhan, S. Wang, B. Yao, X. Hu, X. Song, M. Zhang, X. Wei, Y. Xiong, W. Lu, Liposome-Based Systemic Glioma-Targeted Drug Delivery Enabled by All-d Peptides, ACS Appl. Mater. Inter. 8(2016) 29977-29985.

[30] O. WARBURG, On the origin of cancer cells, Science 123(1956) 309-314.

[31] Q.L. He, I. Minn, Q. Wang, P. Xu, S.A. Head, E. Datan, B. Yu, M.G. Pomper, J.O. Liu, Targeted Delivery and Sustained Antitumor Activity of Triptolide through Glucose Conjugation, Angew. Chem. Int. Ed. Engl. 55(2016) 12035-12039.

[32] A. Starzec, R. Vassy, A. Martin, M. Lecouvey, M. Di Benedetto, M. Crepin, G.Y. Perret, Antiangiogenic and antitumor activities of peptide inhibiting the vascular endothelial growth factor binding to neuropilin-1, Life Sci. 79(2006) 2370-2381.

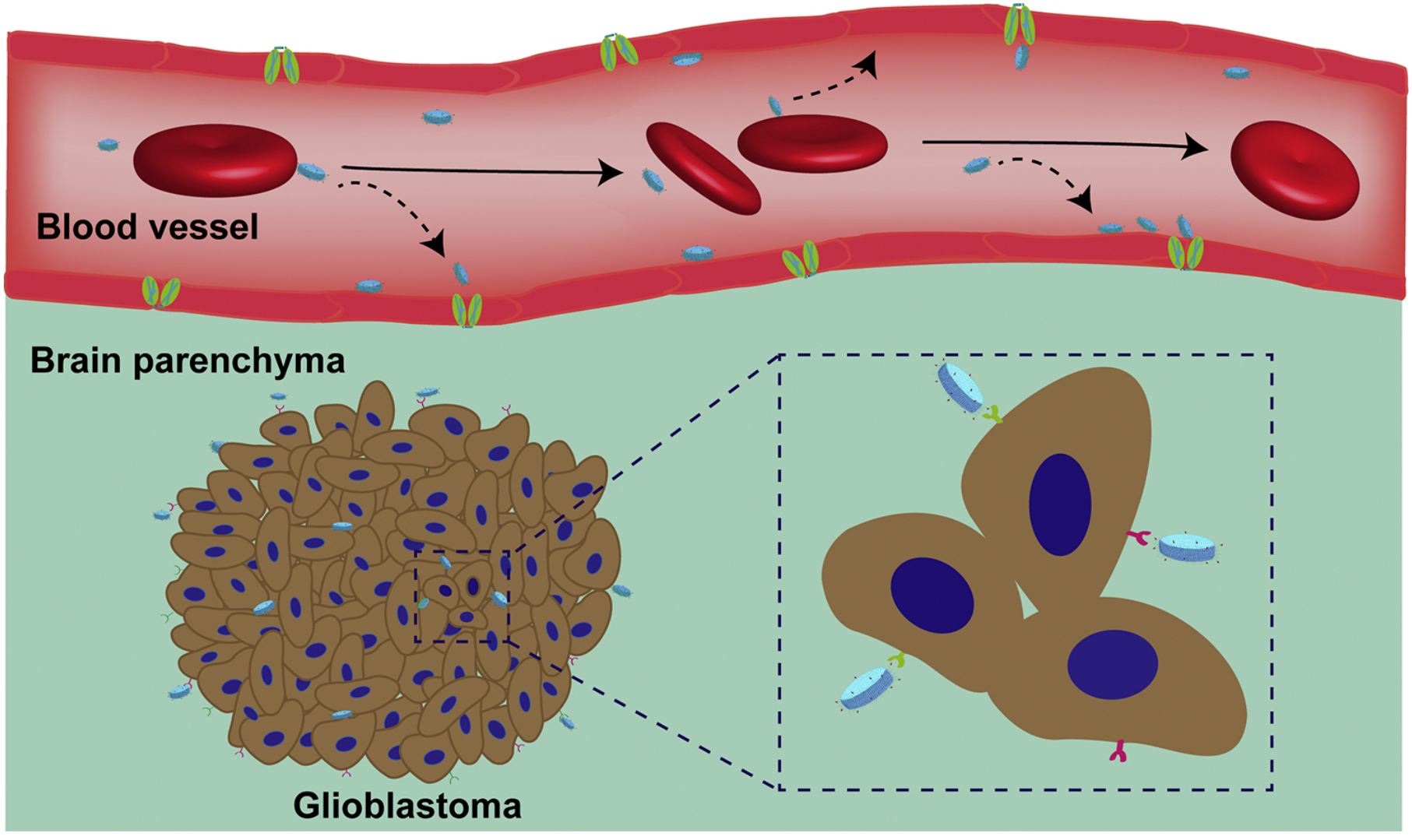

Graphics Abstract

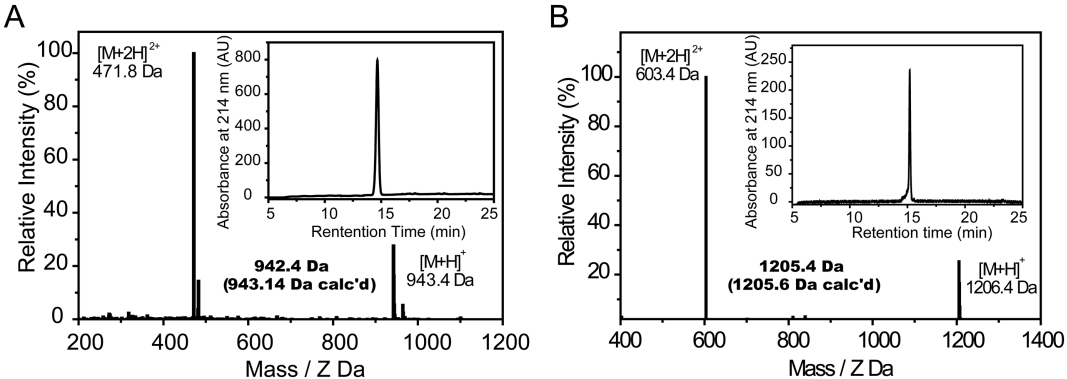
A
[M+2H]2+
471.8 Da
Relative Intensity (%)
Absorbance at 214 nm (AU)
Rentention Time (min)
942.4 Da
(943.14 Da calc'd)
[M+H]+
943.4 Da
Mass / Z Da
B
[M+2H]2+
603.4 Da
Relative Intensity (%)
Absorbance at 214 nm (AU)
Retention time (min)
1205.4 Da
(1205.6 Da calc'd)
[M+H]+
1206.4 Da
Mass / Z Da

Figure 1

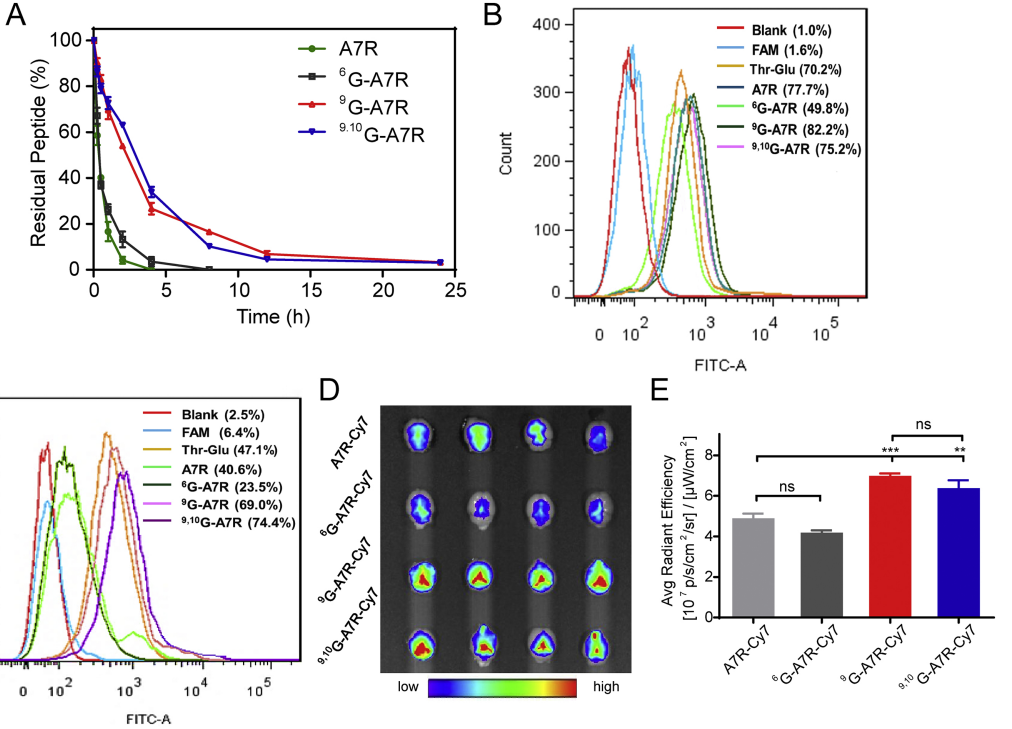
A
Residual Peptide (%)
Time (h)
A7R
6G-A7R
9G-A7R
9,10G-A7R
B
Count
FITC-A
Blank (1.0%)
FAM (1.6%)
Thr-Glu (70.2%)
A7R (77.7%)
6G-A7R (49.8%)
9G-A7R (82.2%)
9,10G-A7R (75.2%)
C
Count
FITC-A
Blank (2.5%)
FAM (6.4%)
Thr-Glu (47.1%)
A7R (40.6%)
6G-A7R (23.5%)
9G-A7R (69.0%)
9,10G-A7R (74.4%)
D
A7R-Cy7
6G-A7R-Cy7
9G-A7R-Cy7
9,10G-A7R-Cy7
low
high
E
Avg Radiant Efficiency
[10 7 p/s/cm 2/sr] / [μW/cm 2]
ns
***
**
ns
A7R-Cy7
6G-A7R-Cy7
9G-A7R-Cy7
9,10 G-A7R-Cy7

Figure 2

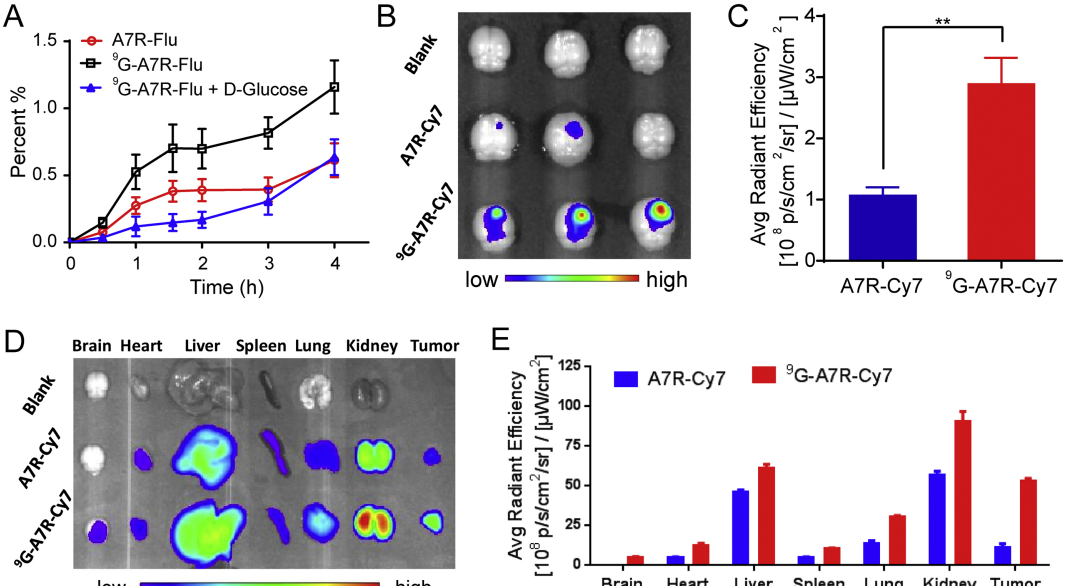
A
A7R-Flu
9G-A7R-Flu
9G-A7R-Flu + D-Glucose
Percent %
Time (h)
B
Blank
A7R-Cy7
9G-A7R-Cy7
low
high
C
Avg Radiant Efficiency [10 8 p/s/cm 2/sr] / [μW/cm 2]
**
A7R-Cy7
9G-A7R-Cy7
D
Brain Heart Liver Spleen Lung Kidney Tumor
Blank
A7R-Cy7
9G-A7R-Cy7
low
high
E
A7R-Cy7
9G-A7R-Cy7
Avg Radiant Efficiency [10^8 p/s/cm^2/sr] / [μW/cm^2]
Brain Heart Liver Spleen Lung Kidney Tumor

Figure 3

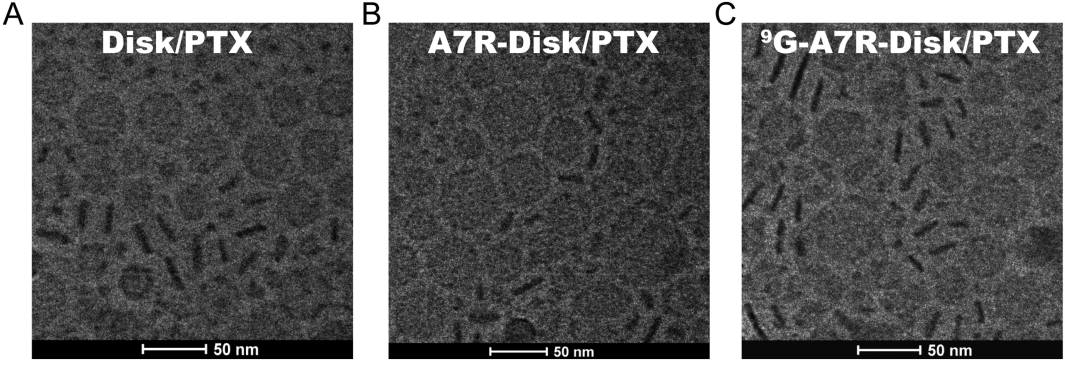

Figure 4

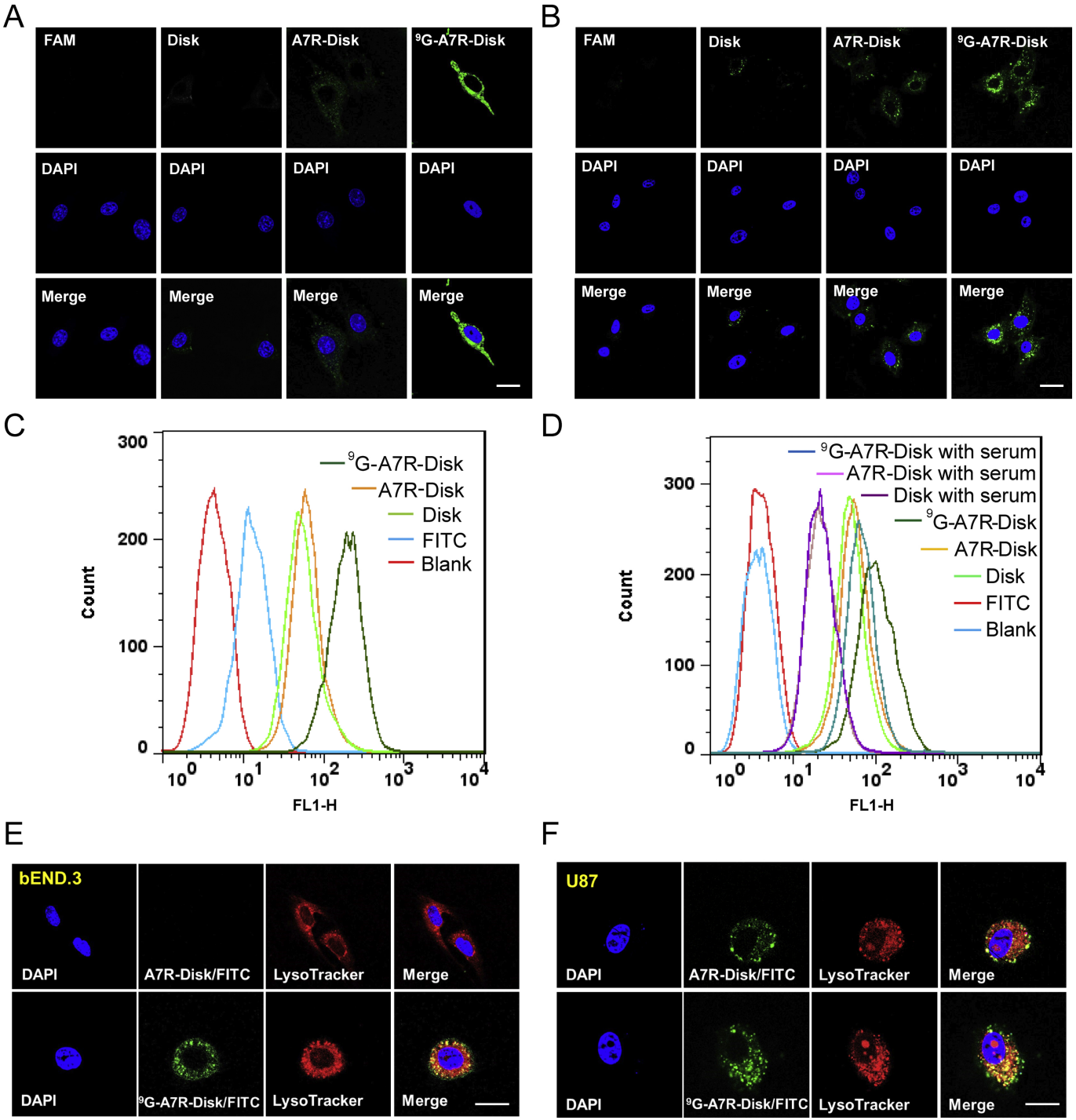
A
FAM
Disk
A7R-Disk
9G-A7R-Disk
DAPI
Merge
B
C
Count
FL1-H
9G-A7R-Disk
A7R-Disk
Disk
FITC
Blank
D
9G-A7R-Disk with serum
A7R-Disk with serum
Disk with serum
E
bEND.3
DAPI
A7R-Disk/FITC
LysoTracker
Merge
9G-A7R-Disk/FITC
F
U87

Figure 5

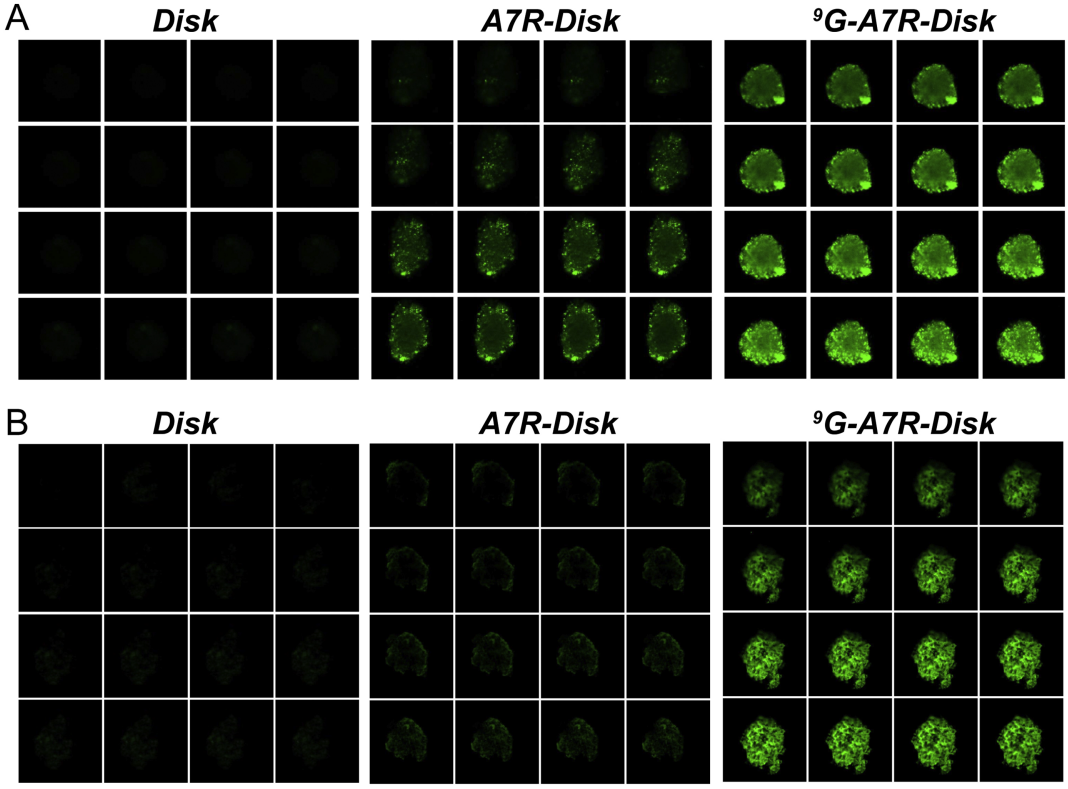

Figure 6

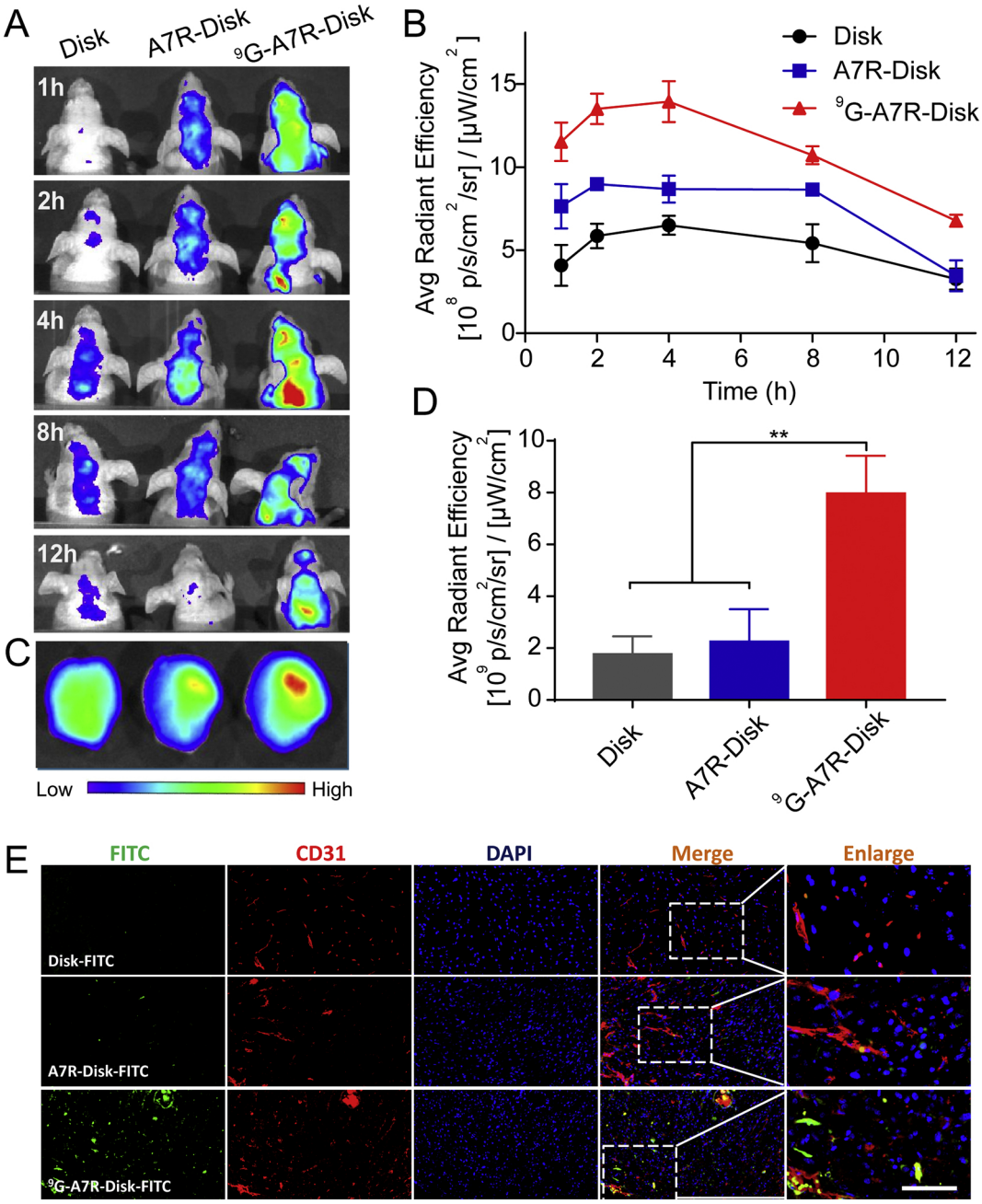
A
Disk
A7R-Disk
9G-A7R-Disk
1h
2h
4h
8h
12h
B
Disk
A7R-Disk
9G-A7R-Disk
Avg Radiant Efficiency
[10^8 p/s/cm^2/sr] / [μW/cm^2]
Time (h)
C
Low
High
D
Avg Radiant Efficiency
[10^9 p/s/cm^2/sr] / [μW/cm^2]
**
Disk
A7R-Disk
9G-A7R-Disk
E
FITC
CD31
DAPI
Merge
Enlarge
Disk-FITC
A7R-Disk-FITC
9G-A7R-Disk-FITC

Figure 7

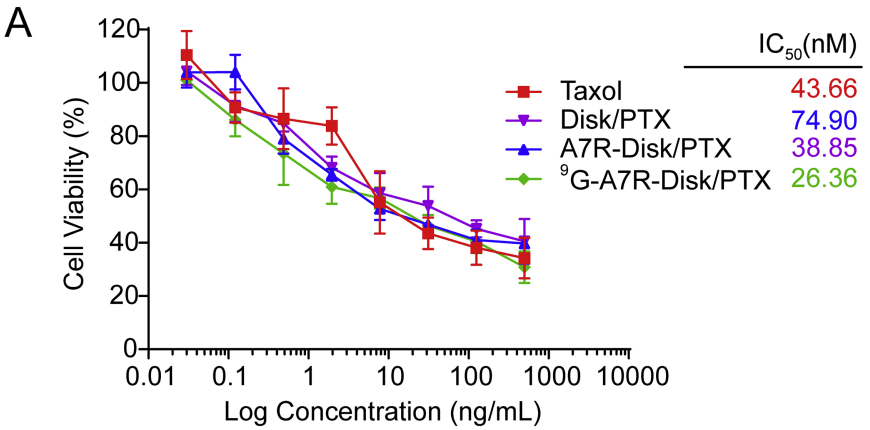
A
Cell Viability (%)
120
100
80
60
40
20
0
0.01
0.1
1
10
100
1000
10000
Log Concentration (ng/mL)
IC50(nM)
Taxol 43.66
Disk/PTX 74.90
A7R-Disk/PTX 38.85
9G-A7R-Disk/PTX 26.36

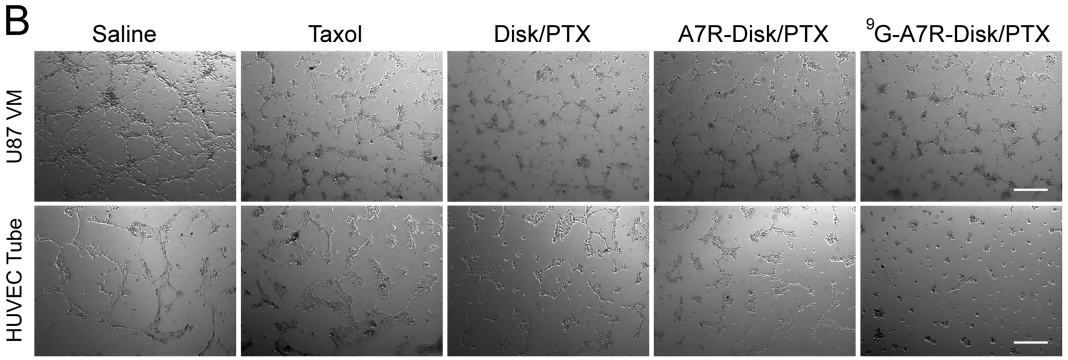
B
Saline
Taxol
Disk/PTX
A7R-Disk/PTX
9G-A7R-Disk/PTX
U87 VM
HUVEC Tube

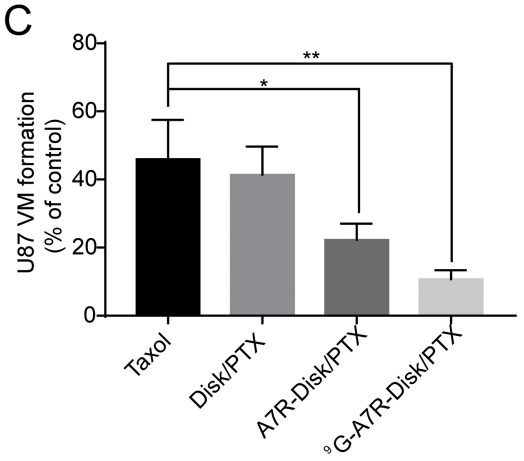
C
U87 VM formation (% of control)
80
60
40
20
0
**
*
Taxol
Disk/PTX
A7R-Disk/PTX
9G-A7R-Disk/PTX

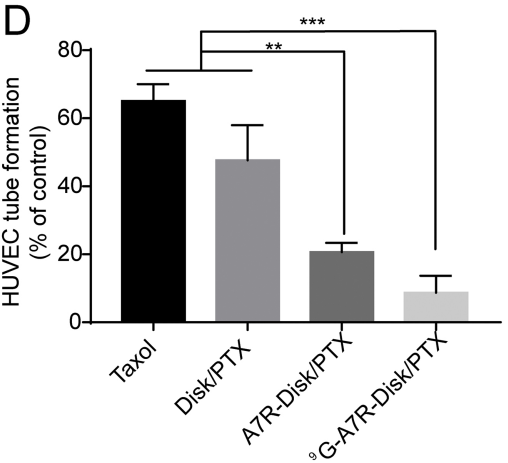
D
HUVEC tube formation (% of control)
80
60
40
20
0
***
**
Taxol
Disk/PTX
A7R-Disk/PTX
9G-A7R-Disk/PTX

Figure 8

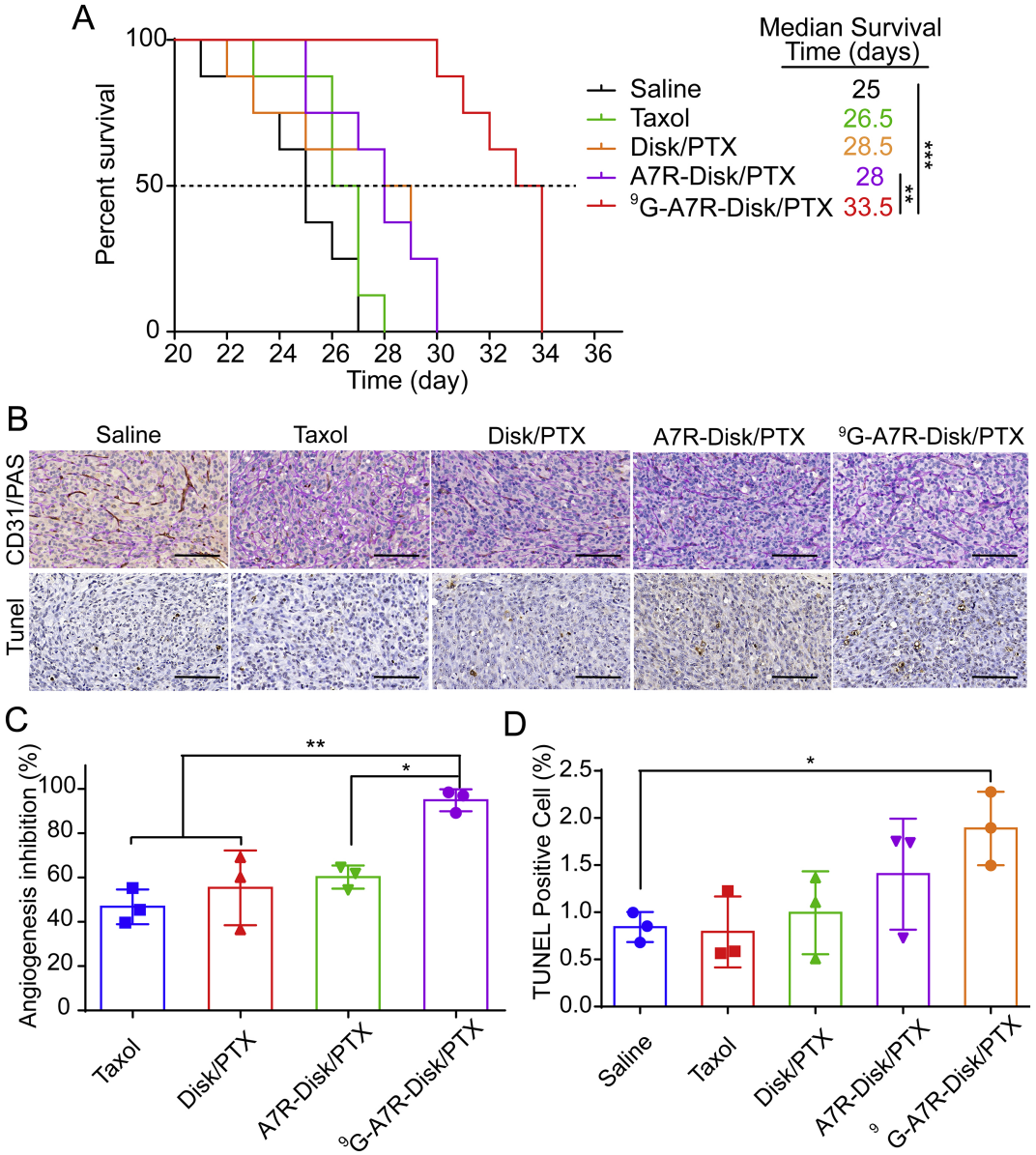
A
Percent survival
100
50
0
20
22
24
26
28
30
32
34
36
Time (day)
Median Survival Time (days)
Saline 25
Taxol 26.5
Disk/PTX 28.5
A7R-Disk/PTX 28
9G-A7R-Disk/PTX 33.5
***
**
B
Saline
Taxol
Disk/PTX
A7R-Disk/PTX
9G-A7R-Disk/PTX
CD31/PAS
Tunel
C
Angiogenesis inhibition (%)
100
80
60
40
20
0
**
*
Taxol
Disk/PTX
A7R-Disk/PTX
9G-A7R-Disk/PTX
D
TUNEL Positive Cell (%)
2.5
2.0
1.5
1.0
0.5
0.0
*
Saline
Taxol
Disk/PTX
A7R-Disk/PTX
9 G-A7R-Disk/PTX

Figure 9